PHOTONICS Research

Hybrid integrated low-noise linear chirp frequency-modulated continuous-wave laser source based on self-injection to an external cavity

Liwei Tang,[1,2] Hongxiang Jia,[1,2] Shuai Shao,[1,2] Sigang Yang,[1,2] Hongwei Chen,[1,2] and Minghua Chen[1,2,*]

[1]Department of Electronic Engineering, Tsinghua University, Beijing 100084, China
[2]Beijing National Research Center for Information Science and Technology (BNRist), Beijing 100084, China
*Corresponding author: chenmh@tsinghua.edu.cn

A hybrid integrated low-noise linear chirp frequency-modulated continuous-wave (FMCW) laser source with a wide frequency bandwidth is demonstrated. By employing two-dimensional thermal tuning, the laser source shows frequency modulation bandwidth of 10.3 GHz at 100 Hz chirped frequency and 5.6 GHz at 1 kHz chirped frequency. The intrinsic linewidth of 49.9 Hz with 42 GHz continuous frequency tuning bandwidth is measured under static operation. Furthermore, by pre-distortion linearization of the laser source, it can distinguish 3 m length difference at 45 km distance in the fiber length measurement experiment, demonstrating its application potential in ultra-long fiber sensing and FMCW light detection and ranging. © 2021 Chinese Laser Press

1. INTRODUCTION

The frequency-modulated laser source is the essential equipment of many detection systems, such as the frequency-modulated continuous-wave (FMCW) light detection and ranging (LiDAR), pulse compression LiDAR, large-band linearly chirped microwave generation, and coherent optical frequency domain reflectometry (OFDR) [1–4]. Compared with the conventional time-of-flight LiDAR, the FMCW LiDAR has more promising performance in autonomous vehicles and aerial photography due to its advantages of eye-safe continuous power, high repetition frequency, and simultaneous measurement of velocity and location [5]. For FMCW coherent detection, the range resolution is relative to the frequency bandwidth and the frequency modulation linearity. A relatively longer chirped period provides abundant energy accumulation and improves the signal-to-noise ratio (SNR) of the detected echo beat signal. The time-bandwidth product (TBWP) of the generated microwave can adequately describe this characteristic [6]. Moreover, the narrow linewidth or low-frequency noise of the LiDAR source provides a high coherent range and increases the potential detectable distance.

However, it is not easy for the FMCW laser source to simultaneously satisfy narrow linewidth, high chirp linearity, and large TBWP. The famous Fourier-domain mode-locked laser realizes 100 nm tuning bandwidth with coherent continuous

sweeping [7]. Nevertheless, it fails to achieve a low-frequency noise because the distributed environmental perturbations will induce phase fluctuations of the stored longitudinal modes in tens of kilometers of fiber. The chirped temporal duration should be equal to the long fiber time delay, so the severe instability is induced, and the TBWP thus is limited to 1.5×10^6 [8,9].

With the development of silicon photonics technology, it is a trend to reduce the linewidth by coupling the high-quality (high-Q) microresonator with a semiconductor laser. By self-injection locking, the formed compound cavity can prolong the photon lifetime, suppress the amplified spontaneous emission noise, reduce the spectral linewidth, and improve the coherent time. A high-Q whispering gallery mode microresonator coupled with a distributed feedback (DFB) laser is used to achieve the sub-100 Hz linewidth [10]. However, their laser has no frequency modulation functions under the self-injection locked state.

In this paper, an FMCW laser source based on a self-injection locked commercial DFB laser diode (LD) coupled with a high-Q Si_3N_4 microring resonator (MRR) is demonstrated, which achieves large bandwidth with linear frequency modulation based on the phase-MRR two-dimensional tuning method. The 49.9 Hz intrinsic linewidth and 2.6 kHz integral linewidth with continuous tuning bandwidth up to 42 GHz can be achieved under static operation. For dynamic

FMCW tuning, it achieves 10.3 GHz with a chirped frequency of 100 Hz and 5.6 GHz with a chirped frequency of 1 kHz. The TBWP of the generated microwave waveform is up to 5.1×10^7. By pre-distortion linearization of the FMCW laser source, the length difference of 3 m at 45 km distance can be distinguished without the compensation algorithm in the fiber length measurement experiment. With such a low noise and high linearity FMCW laser source, optical fiber sensing and the LiDAR system will be further developed.

2. PRINCIPLE

As shown in Fig. 1, the proposed FMCW laser source consists of a DFB LD and an external MRR. The MRR is designed as the add-drop single ring type, of which the input and drop ports are connected through a multimode interferometer (MMI). The output port of the MRR is coupled to a single-mode fiber (SMF) as the output of the laser source, while another add port of the MRR is left connected. On the top of the waveguides, two thermal detuning electrodes are fabricated, one of which is on the input waveguide before the MMI for detuning the phase delay, and another is on the ring waveguide for detuning the central resonant frequency. Sufficient optical feedback from the MRR is injected into the DFB laser, enabling a significant spectral linewidth reduction.

The effect of self-injection has been well studied. It can be divided into five regimes depending on the feedback ratio [11]. From low to high feedback ratio, the regimes are described as Regime I to Regime V. The feedback strength can be improved when the MRR central resonant frequency is close to the solitary frequency of DFB by tuning the MRR electrode. When the feedback ratio exceeds 10%, the DFB laser enters the Regime V, showing a stable single-longitudinal mode output with narrow linewidth. Under this state, the role of the MRR in the FMCW laser can be simplified into two parameters, viz. the full width at half-maximum (FWHM) spectral linewidth Λ at the central resonant frequency, and the resonant frequency ω_f, which is defined as the frequency offset from the solitary laser. The frequency-dependent complex reflection coefficient of the MRR can be expressed by the Lorentz function [12]:

$$\Gamma(\omega) = \frac{\Lambda}{\Lambda - i(\omega - \omega_f)}. \tag{1}$$

The dynamical response of the self-injected laser can be described by the equation [13]

$$(\omega - \omega_0)\tau = -C_{\text{eff}} \sin\left[\omega\tau + \arctan(\alpha) - \arctan\left(\frac{\omega - \omega_f}{\Lambda}\right)\right], \tag{2}$$

where

$$C_{\text{eff}} = \frac{\gamma\tau\Lambda\sqrt{1 + \alpha^2}}{\sqrt{\Lambda^2 + (\omega - \omega_f)^2}}, \tag{3}$$

represents the effective optical feedback efficiency. ω_0 and ω represent the solitary frequency of the laser diode and the operating frequency of the output mode, respectively. τ is the external round-trip time, γ is the feedback rate, and α is the linewidth enhancement factor. $\psi = \omega\tau + \arctan(\alpha)$ represents the external phase delay. Without loss of generality, ψ can be represented by $\psi_0 + \omega\tau$. As for the proposed hybrid laser, the ψ_0 and ω_f can be detuned by the phase and MRR thermal electrodes, respectively.

The locking state is the result of the synchronous tuning of the phase and MRR electrodes, which can be explained by solving the relationship between ω_f and ω in Eq. (2). Figure 2 shows the solution of ω with respect to ω_f at the phase delay $\psi_0 = 2\pi/3$. The parameters of the devices are taken from the typical values [14]. When tuning ω_f from low to high, the figure shows that the output frequency ω will follow the change of ω_f and jump to the locked area near the resonance frequency ($\omega_f = 0$ GHz). In the locked area, ω can be modulated proportional to ω_f (the slope of the curve is 1). This tuning process corresponds to the different regimes of the laser under different optical feedback intensities where the output mode evolves from a multimode, mode-locked, and chaotic state to a stable single-longitudinal mode state [15]. Figure 2 also shows the hysteresis effect, which is expected in the self-injected laser [16]. When tuning the ω_f to the locked area, the ω_f can be tuned back lower for maximum frequency tuning band.
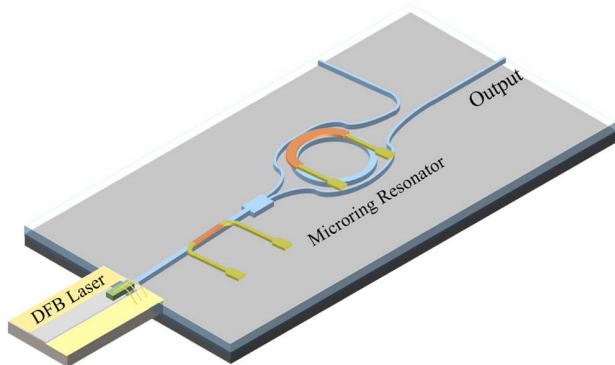

Fig. 1. Schematic diagram of the proposed hybrid FMCM laser source. The DFB laser is coupled with an MRR where the blue lines represent the waveguides; the red lines represent the phase and MRR electrodes.
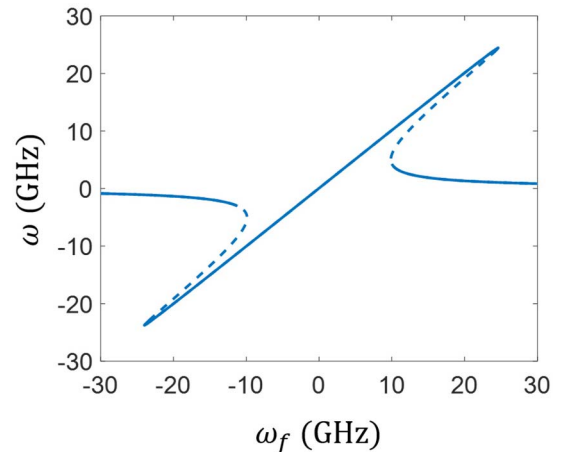

Fig. 2. Output frequency detuning with respect to the MRR resonance frequency.

And the similar effect occurs when the ω_f is tuned from high to low frequency.

Under the locked state, the linear frequency-modulated area only appears if the external round-trip time is less than a specific value. Figure 2 is plotted with the external round-trip time $\tau = 50$ ps, while the multiple solutions will appear when τ increases to 500 ps. The longer external cavity tolerates multiple mode resonances and accumulates outer disturbances, which is unfavorable for continuous frequency tuning under a self-injection locked state. The silicon photonics integrated waveguide platform provides the opportunity of a short cavity, whose compact size can easily shorten the length of the external cavity to less than 10 mm. In order to avoid mode hopping and obtain a maximum tuning bandwidth, another tuning factor that needs to consider is the phase delay ψ_0. When tuning ω_f, the external cavity will restrict the phase space of the self-injected laser. The phase delay ψ_0 needs to be tuned with ω_f to compensate for the phase detuning caused by the external cavity. Therefore, the phase-MRR two-dimensional tuning should be employed for maximum FMCW bandwidth.

3. DESIGN AND FABRICATION

The MRR is fabricated based on the Si_3N_4 waveguide platform, which is suitable for designing the FMCW laser source.

First, the Si_3N_4 waveguide is transparent in the spectral range of 400–2350 nm [17] and can be freely applied to LiDAR laser sources in different wavelength bands [18]. Second, the low-loss propagation waveguide can be used to fabricate high-Q resonators, which is essential for narrowing the intrinsic linewidth of the LD. Third, the Si_3N_4 waveguide has a high-aspect-ratio cross section [19]. The aspect ratio of the fundamental mode it supports matches well with the mode of the DFB laser. Therefore, the DFB laser can be butt coupled to the external cavity to obtain high coupling efficiency. The high coupling efficiency introduces a high optical feedback ratio, which allows the DFB to enter the self-injection locked state. In addition, the Si_3N_4 material has a relatively low thermo-optic coefficient, which is helpful to improve the long-term thermal stability of the FMCW laser source [20].

The employed Si_3N_4 waveguide platform has been introduced in our previous work [21,22]. As shown in Fig. 3(a), the 100 nm thick Si_3N_4 layer is grown on the 10 μm thick thermal oxide SiO_2 layer. The Si_3N_4 layers are deposited by low-pressure chemical vapor deposition (LPCVD) and waveguides are etched by 180 nm resolution lithography. The pattern mask is fabricated by reactive ion plasma etching. The etched Si_3N_4 waveguides are buried by a 2 μm thick LPCVD SiO_2 and a 6 μm thick plasma-enhanced chemical
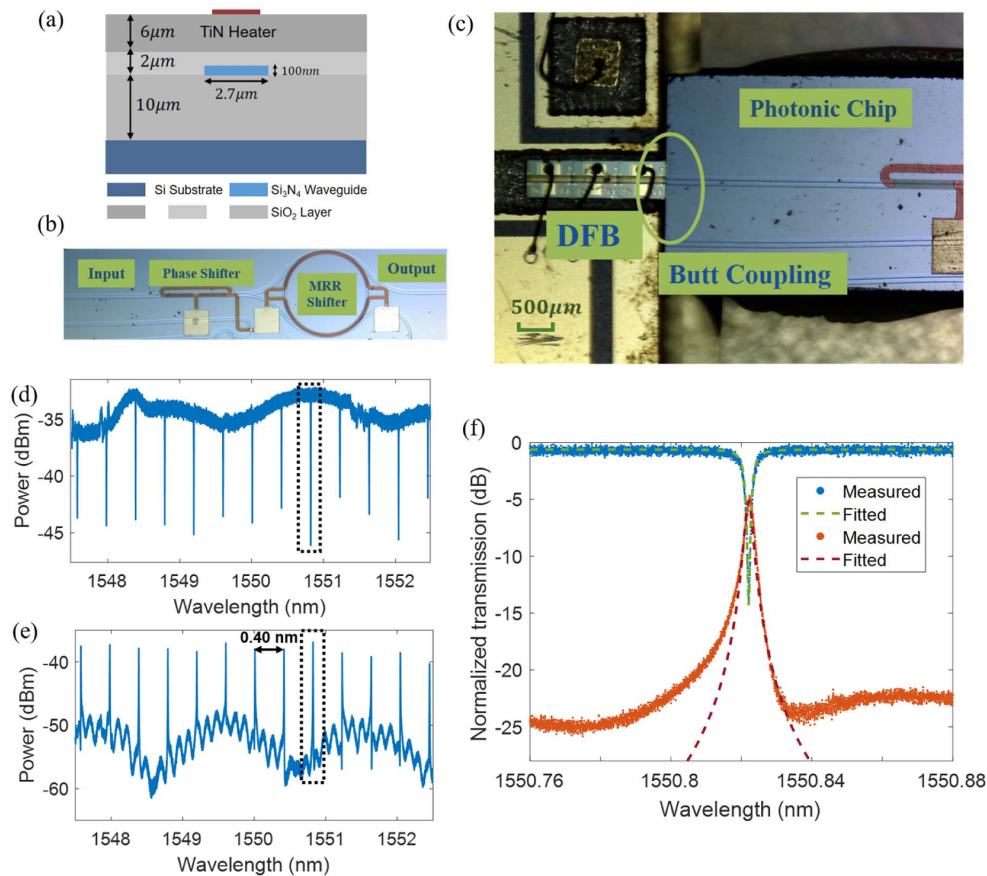

Fig. 3. (a) Cross-section schematic of the Si_3N_4 waveguide platform. (b) Microscope photo of the fabricated MRR. (c) Microscope photo of the hybrid laser. (d) Measured transmission spectra from the input port to the output port of the MRR. (e) Measured reflection spectra at the input port of the MRR with an FSR of 0.40 nm, equivalent to 50 GHz. (f) Enlarged view of transmission and reflection spectra of the dashed line in (d) and (e) where the measured data and Lorentz-type fitted curve are plotted by dots and dashed lines.

vapor deposition (PECVD) SiO_2 cladding layer. The TiN thermal tuning electrodes are deposited on the top of the waveguide.

As for the design of the MRR, the waveguide width is optimized to 2.7 μm for the low-loss TE mode propagation. The FWHM of the cold laser cavity of the DFB laser diode is about 50 GHz [10]. Therefore, the ring is designed to be 1.2 mm in diameter to achieve an free spectral range (FSR) of 50 GHz so that only one single feedback resonant frequency of the MRR is allowed in the bandwidth of the cold cavity to avoid multimode resonance. The gap between the ring waveguide and the bus waveguide is optimized to be 1 μm for high phase delay. The input waveguide is designed as a spot-size converter (SSC) to match the mode field shape of the DFB. The fabricated MRR is demonstrated in Fig. 3(b).

The transmission and reflection spectra of the MRR are measured by the advanced optical spectrum analyzer (OSA, APEX 2081), which has a built-in broadband tunable laser source with a spectral resolution of 0.16 pm (equivalent to 20 MHz) and a bandwidth that covers the whole C-band. Figures 3(d) and 3(e) demonstrate the transmission spectra and reflection spectra at 1550 nm with a 5 nm span, showing an FSR of 0.40 nm (equivalent to 50 GHz). The enlarged view of the spectra near 1551 nm is plotted in Fig. 3(e), where the Lorentz-type function is employed to fit the curve [23]. The FWHM of the spectra is 310 MHz, and the Q value is calculated to be 6.2×10^5.

The DFB laser diode is commercially available, and the butt coupling is employed in this hybrid laser source, as shown in Fig. 3(c). The SSC is a straight waveguide with a gradually narrower width, which has reduced the butt-coupling loss to be less than –2.5 dB, allowing sufficient optical feedback to the DFB laser diode (>10 % feedback ratio). The output field of the integrated waveguide is guided by a group of collimating lenses and a lensed fiber in an SMF. An optical isolator is placed between them to prevent external reflections. In addition, thermistor and thermoelectric cooling are employed, which are not shown in Fig. 3(c).

4. EXPERIMENTAL RESULTS

A. Static Operation

The packaged hybrid laser is first tested under the DC pumping state, the test scheme of which is shown in Fig. 4(a). By adjusting the phase and MRR voltages, the output mode evolves to a self-injection locked state from a multimode, chaotic state, whose spectra are monitored by the OSA [24]. Figure 4(b) shows the self-injection locked state at 1548.6 nm, showing a single-longitudinal mode with a side-mode suppression ratio (SMSR) of 50 dB. Under self-injection locked state, tuning MRR, and phase electrodes, the wavelength is shifted continuously from 1548.631 nm to 1548.928 nm, equivalent to 42 GHz frequency bandwidth. The optical power in the fiber is 0 dBm, while the free-running power is 10 dBm. The lost power is mainly from the following four aspects. (1) The edge butt coupling loss between the DFB and silicon photonic chip is –2.5 dB. (2) Under the locked state, the oscillating mode is near the resonant frequency of the MRR. Therefore, the power coupling loss from the bus waveguide to the ring waveguide is estimated to be about 3 dB. (3) The add port of the MRR in the design is left unconnected, which has a 3 dB loss. (4) Coupling from the silicon photonic chip to the SMF has a loss of 1 dB. In our design, the drop port and output port are not connected by the MMI to avoid interference effects and internal backreflections. The research has shown that the self-injection locked state has strong
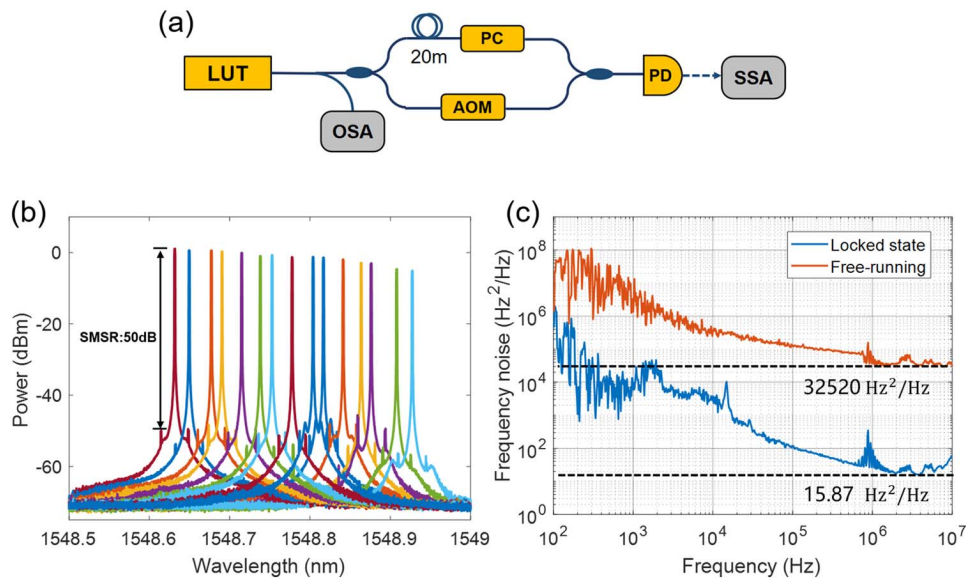

Fig. 4. (a) Experimental diagram of the test scheme. LUT, laser under test; PC, polarization controller. (b) The output spectra under static continuous frequency tuning. By tuning the phase and MRR electrode, the wavelength is detuned from 1548.631 nm to 1548.928 nm with an SMSR of 50 dB. (c) Frequency noise spectrum from 100 Hz to 10 MHz at static operation. The red and blue lines are frequency noise spectrum during free-running and self-injection locked operation, respectively. White frequency noise of free-running and self-injection locked states is respectively marked out in the figure.

stability and anti-interference [25]. It has the potential to increase 3 dB fiber power by connecting the two ports.

The spectral characteristics of the static output are measured with the scheme where an unbalanced Mach–Zehnder interferometer (MZI) is used to obtain the laser frequency discriminating spectrum at a self-injection locked state [26]. As shown in Fig. 4(a), the length difference between the two arms is 20 m. The acousto-optic modulator is placed on the shorter arm to prevent homodyne interference. After photodiode (PD) envelope detection, the output signal is fed into the signal source analyzer (SSA, E5052B, Keysight). The unbalanced MZI has a sub-coherence time delay, and the fluctuation of the laser frequency is converted into the phase fluctuation of the beat note. The frequency noise and intrinsic laser linewidth can be identified by analyzing the heterodyne beat note's phase noise spectral density (PNSD). This advanced measurement setup is similar to the more widely used delayed self-heterodyne interferometer (DSHI) [27]. However, for ultra-narrow linewidth evaluation, the DSHI scheme has lost its accuracy, and the measurement of frequency noise is more reasonable, which has been analyzed in detail [28,29].

The SSA obtains the single-sideband power spectral density $S_{\Delta\varphi}(f)$ of the delayed laser phase noise, where $\Delta\varphi = \varphi(t) - \varphi(t - \tau)$ and τ is the time delay between the two arms. The instantaneous laser frequency noise can be derived by [28]

$$S_\nu(f) = \frac{f^2}{4[\sin(\pi f \tau)]^2} S_{\Delta\varphi}(f). \tag{4}$$

The frequency noise spectra $S_\nu(f)$ of the free-running and self-injection locked states from 100 Hz to 10 MHz are plotted in Fig. 4(c). The white noise is dominant in the high-frequency range, mainly caused by the random spontaneous emission and carrier fluctuation, which is the so-called "quantum-noise" process that determines the Lorentzian-type shape. In the spectrum, the intrinsic linewidth directly refers to

$$\Delta\nu_{\text{intrinsic}} = \pi S_\nu^0, \tag{5}$$

where S_ν^0 is the single-sideband power spectral density of white frequency noise. In Fig. 4(c), the S_ν^0 of the free-running and self-injection locked states is read to be 32,520 Hz^2/Hz and 15.87 Hz^2/Hz, respectively. So the intrinsic linewidth is calculated to be 102.2 kHz and 49.9 Hz, respectively. The linewidth has been suppressed by 3000 times under the self-injection locked state compared to the free-running state. This improvement derives from the optical feedback of the high-Q external cavity, which provides a long photon lifetime and suppresses spontaneous emission noise [30].

The low-frequency noise is dominant in coherent detection applications such as FMCW LiDAR and OFDR fiber sensing. The broadened frequency spectrum near the central frequency is mainly coming from the low-frequency noise. The integrated linewidth can represent the low-frequency noise, which can be obtained by integrating the frequency noise:

$$\int_{\Delta\nu_{\text{int}}}^{\infty} \frac{S_\nu(f)}{f^2} \, df = \frac{1}{\pi} \ \text{rad}^2, \tag{6}$$

where $S_\nu(f)/f^2$ represents the laser phase noise, and $\Delta\nu_{\text{int}}$ is the effective integral linewidth, approximated to be the low Fourier frequency which is the value of phase noise integration

equal to unity. In Fig. 4(c), the $\Delta\nu_{\text{int}}$ solutions for the free-running and self-injection locked states are 70.0 kHz and 2.6 kHz, respectively. The integral linewidth is more applicable in metrology and sensing. Compared with suppressing spontaneous emission to reduce intrinsic linewidth, it has more operable suppression methods. For example, electrical feedback becomes an effective method to reduce the frequency noise within the loop bandwidth [31].

The PNSD in Fig. 4(c) is measured at a fixed point in the locked state. When the wavelength is redshift from 1548.8 nm, the output power is gradually dropped. It is the state before mode hopping where the locked position of the MRR has shifted. However, within the whole 42 GHz tunable band, the PNSD still maintains a low-frequency noise as Fig. 4(c) shows. The intrinsic and integral linewidth has not observed significant change. The single oscillating longitudinal mode and SMSR are maintained in the whole tunable band. For the dynamical system like the self-injection locked laser, the switching of the operation state is abrupt. Only when the wavelength exceeds 1548.928 nm, the mode hopping will occur immediately. It will maintain a stable narrow linewidth output within the locked area, whether under static or dynamic modulation. As mentioned above, the hysteresis effect under the locked Regime V expands the locking range. Once locked, the narrow linewidth, single oscillating mode, will remain until the next state is switched. Thus, a continuously tuning bandwidth of up to 42 GHz can be achieved within the locked band.

B. Linearly Chirped FMCW
In Fig. 4(a), the 42 GHz continuous frequency tuning band is obtained. For stable linearly chirped FMCW, select the wavelength bands from 1548.65 nm to 1548.79 nm (equivalent to 18 GHz) as the modulated bands. When the tuning range exceeds 1548.8 nm, the power decreases. Although it is still a stable single-longitudinal mode operation, there is a risk of mode hopping during fast frequency modulation. Figure 5(a) demonstrates the frequency detuning from 1548.65 nm with respect to MRR and phase tuning voltage. The resistance of phase and MRR electrodes is 78 Ω and 274 Ω, respectively. Therefore, the maximum power consumption of phase and MRR heaters is 304 mW and 252 mW, respectively. The output power drops when the frequency is lower than 5 GHz. The reason may be that the locked position is not stable. Although there is a sufficient ratio of optical feedback to enable strong self-injection locking, the lasing frequency fails to maintain stable tuning with the MRR's resonant frequency. So the power is reduced due to the filtering effect of the MRR. As the aforementioned two-dimensional tuning method, the MRR is mainly used to tune the output frequency while the phase electrode is used for compensation. If the phase compensation is not keeping up with the MRR, the mode hopping will occur. So the phase delay ψ_0 should be proportional to ω_f and the voltage V_p should also be linear with V_{mrr}, whose relationship can also be derived from the measured data in Fig. 5(a). Therefore, the driving voltage V_p can be represented by V_{mrr}:

$$V_p = kV_{\text{mrr}}, \tag{7}$$

where k is the proportional coefficient. The square of the voltage represents the thermal power. It is known that the resonant
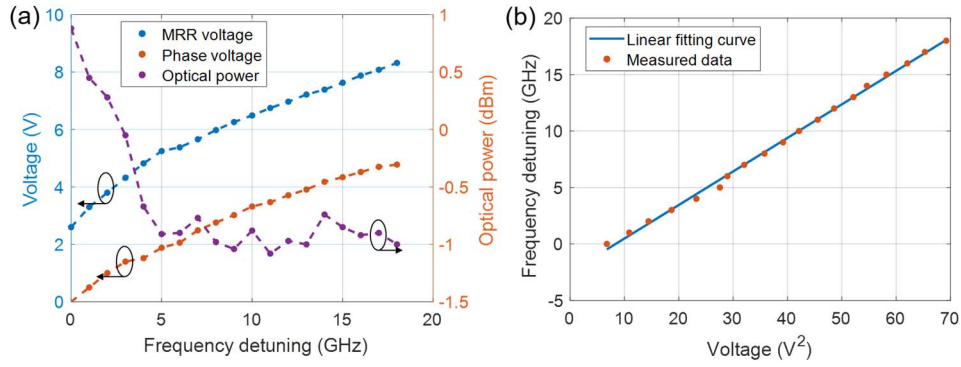
Fig. 5. Characteristics of continuous frequency tuning. (a) MRR and phase tuning voltage and output power corresponding to the detuning frequency. The measured wavelength band is from 1548.65 nm to 1548.79 nm. The *x* axis represents a frequency offset from 1548.65 nm. Starting from 1548 nm, at intervals of 1 GHz, the output power and detuning voltage are recorded in the diagram. (b) The detuning frequency with respect to the MRR detuning power. The square of the MRR voltage represents the thermal power.

frequency of the MRR is linear with the thermal power. Figure 5(b) illustrates that the resonant frequency of the MRR is indeed linear with the detuning frequency, which experimentally proved the linear tuning area shown in Fig. 2. If time-dependent voltages $u_{\mathrm{mrr}}(t)$ and $u_p(t)$ are applied, the time-dependent frequency modulation $\nu(t)$ will be obtained. However, the heat propagation is not instantaneous with time, resulting in the nonlinearity of $\nu(t)$. Linear frequency detuning can be achieved in a static state [shown in Fig. 5(b)], but it cannot be realized in frequency modulation [32]. The heater electrode is fabricated on 8 μm top of the waveguide, whose cross-section structure is shown in Fig. 3(a). The transfer of heat in the cladding delays the time to reach the waveguide and aggravates the nonlinearity of the thermal tuning. As the thickness of SiO₂ cladding increases, there will be more uncertainty. Thinning of the PECVD SiO₂ cladding layer for faster thermal transmission may be an option.

Here, we employ the iterative learning pre-distortion linearization of the hybrid laser source [33]. The schematic is shown in Fig. 6, which has been proven effective in generating periodic modulated signals [34]. The FMCW laser source first passes the 20 m delayed unbalanced MZI to obtain the differential frequency. The PD receives the delayed self-homodyne signal. Then the phase $\varphi_b(t)$ of the beat note is extracted by the Hilbert transform. With short delay time, the $\varphi_b(t)$ can be written as
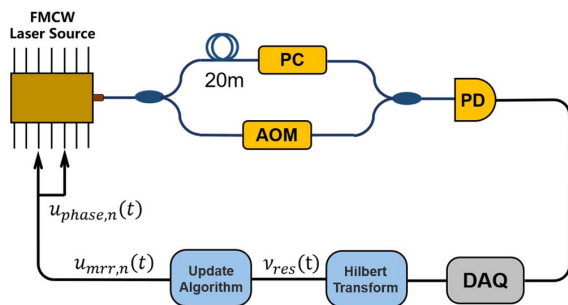
$$\varphi_b(t) = 2\pi\tau\nu(t). \tag{8}$$

However, the obtained $\varphi_b(t)$ is nonlinear with time, and linear fitting should be employed to obtain the desired linear phase $\varphi_d(t)$. Then, the residual nonlinear frequency error can be calculated by

$$\nu_{\mathrm{res}}(t) = \frac{\varphi_b(t) - \varphi_d(t)}{2\pi\tau}. \tag{9}$$

Considering that heat conduction is the first derivative with time, the iterative learning variables need to use derivatives of residual difference $\frac{\mathrm{d}}{\mathrm{d}t}\nu_{\mathrm{res}}(t)$ and $\nu_{\mathrm{res}}(t)$. The nth driver voltage is obtained by iteration:

$$u_{\mathrm{mrr},n}(t) = u_{\mathrm{mrr},n-1}(t) + a\nu_{\mathrm{res}}(t) + b\frac{\mathrm{d}}{\mathrm{d}t}\nu_{\mathrm{res}}(t), \tag{10}$$

where $u_{\mathrm{mrr},n}(t)$ and $u_{\mathrm{mrr},n-1}(t)$ represent the nth and $(n-1)$th driving voltage signal; a and b represent the iterative learning coefficient. The nth time-dependent driving voltage of the phase electrode can be derived by the proportional coefficient from Eq. (7):

$$u_{\mathrm{phase},n}(t) = ku_{\mathrm{mrr},n}(t). \tag{11}$$

The nonlinearity of frequency sweep can also be represented by the linear regression coefficient of determination R^2, and ν_{rms} is defined as the root mean square of the residual frequency $\nu_{\mathrm{res}}(t)$ whose relationship with R^2 has been given in Ref. [2]. Define a region of interest (ROI) as the linearly chirped frequency region at the intermediate chirped band, and neglect the region at the end of each period where the frequency modulation changes significantly. Taking the chirp frequency of 500 Hz as an example, by applying an initial driving voltage $u_{\mathrm{mrr}}(t)$ and $u_{\mathrm{phase}}(t)$, affected by nonlinear thermal modulation, $1 - R^2$ is calculated to be more than 0.2. By 50 iteration cycles, the driving voltage signals of the phase and MRR are updated which are shown in Fig. 7(b), and the residual frequency error is suppressed to less than 3 MHz, as shown in Fig. 7(k). And $1 - R^2$ is calculated as 3.6×10^{-9} and 8.8×10^{-9} of up and down ramps, which is 9 orders of magnitude reduced compared to the initial residual error. The ratio of the ROI to the entire chirped bandwidth of the up ramp and down ramp is
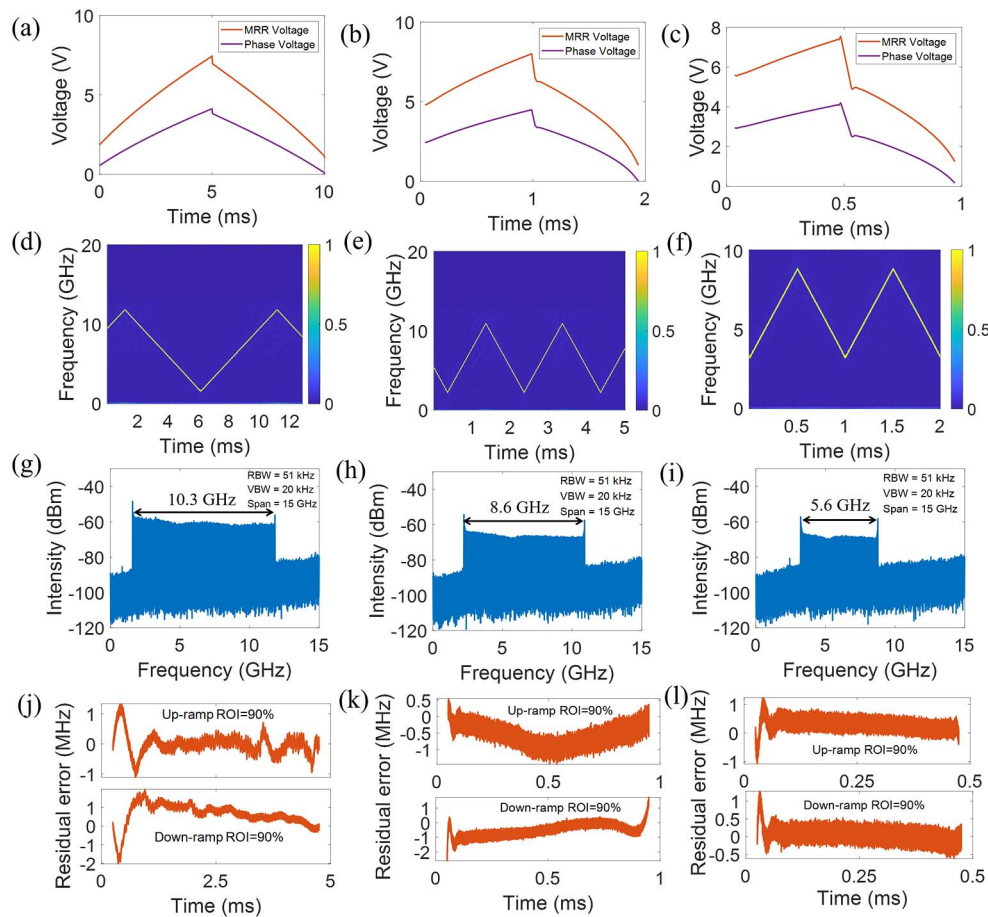

Fig. 6. Schematic of iterative learning pre-distortion linearization.

Fig. 7. (a)–(c) Time-dependent driving voltage of phase and MRR electrodes by iterative learning. (d)–(f) Time-frequency spectrum of the beat note by the FMCW laser source with reference laser. (g)–(i) Frequency spectrum of the heterodyne beat note with RBW = 51 kHz, VBW = 20 kHz, span = 15 GHz. (j)–(l) The residual nonlinear frequency error $\nu_{res}(t)$ of the up ramp and down ramp at a chirped period. The chirped frequency is 100 Hz for (a), (d), (g), (j), 500 Hz for (b), (e), (h), (k), and 1 kHz for (c), (f), (i), (l), respectively.

90%. The short-time Fourier transformed (STFT) time-frequency spectrum of the beat note generated by beating the FMCW laser source with a frequency reference laser (PPCL-550, Pure Photonics) is shown in Fig. 7(e). The chirped frequency bandwidth is 8.6 GHz with a chirped duration of 1 ms, so the chirped rate is 8.6 GHz/ms, where the beat note frequency spectrum is shown in Fig. 7(h) and the generated microwave parameters are listed in Table 1.

In addition, we also demonstrate the experimental results of 100 Hz and 1 kHz chirp frequency. The time-dependent driving voltages they employ are shown in Figs. 7(a)–7(c). The STFT time-frequency spectra are shown in Figs. 7(d)–7(f). The frequency spectra of the beat note by the FMCW laser source

with the reference laser are shown in Figs. 7(g)–7(i). Nonlinear frequency residual errors $\nu_{res}(t)$ of up and down ramps at each period are shown in Figs. 7(j)–7(l). Their parameters are summarized in Table 1. The residual error is different between the different chirped periods. Compared with the chirp period of 500 Hz and 1 kHz, 100 Hz has an unfavorable residual error and worse linearity, demonstrating the different shapes in Fig. 7(j). We speculate that this result is related to the quantization accuracy of the signal generator that generates the driving voltage and the thermal stability of the silicon photonic chip.

With a frequency bandwidth of 10.3 GHz and a sweep speed of 100 Hz, the microwave waveform generates ultra-large

Table 1.   Parameters of the Generated FMCW Signal

			Up Ramp			Down Ramp		
Chirp Frequency (Hz)	Bandwidth (GHz)	Chirp Rate (GHz/ms)	$1 - R^2$	ν_{rms} (MHz)	ROI	$1 - R^2$	ν_{rms} (MHz)	ROI
100	10.3	2.1	3.0×10^{-8}	1.19	90%	2.6×10^{-8}	0.93	90%
500	8.6	8.6	3.6×10^{-9}	0.26	90%	8.8×10^{-9}	0.76	90%
1000	5.6	11.1	5.3×10^{-9}	0.22	90%	4.1×10^{-9}	0.21	90%

TBWP of 5.1×10^7, which is of great significance in improving the SNR of long-distance detection. As is known, the resolution is degraded by broad linewidth and nonlinear frequency modulation. The effect of frequency modulation nonlinearity becomes more evident as the detection distance increases. The detected errors caused by modulation nonlinearity accumulate with the distance increase, and the 3 dB bandwidth of the received signal will linearly expand as the distance. If the frequency modulation is perfectly linear, ν_{rms} can be ignored, and the resolution is only related to the frequency bandwidth $\Delta\nu$ [35]. The resolution calculation equation has degenerated to $\Delta z = c/2\Delta\nu$, which is consistent with the commonly used formula [36]. The proposed FMCW laser source achieves high linear frequency chirp by pre-distortion linearization with wide bandwidth, which has the potential to improve resolution in long-distance detection without compensation [37].

C. Experiment of Fiber Length Measurement

In order to evaluate the performance of the FMCW laser source, the fiber under test (FUT) length measurement experiment is set up, as shown in Fig. 8. Two fibers with lengths of 350 m and 45 km are chosen to be measured. In each measurement, a 3 m fiber is connected to the FUT for testing the distance resolution. Figures 8(b)–8(g) show the Fourier spectrum of the beat note where the x axis has been demodulated into the fiber length. Figures 8(b) and 8(e) are the demodulated spectrum of the up and down ramps for one chirp duration. The measurements of the FUT without an extra 3 m fiber in Figs. 8(b) and 8(e) are 335.61 m and 335.62 m, respectively. The blue line is the experimental result with an extra 3 m fiber, showing measured lengths of 338.65 m and

338.64 m. Therefore, the extra fiber length is calculated as 3.03 m and 3.02 m of the up and down ramps, respectively. The 3 dB bandwidth of each peak is about 0.04 m, which means the theoretical distance resolution at 335.61 m is 0.04 m.

Figures 8(c)–8(g) show the measurements with longer FUT. Without an extra fiber, the measured lengths are 45,376.82 m and 45,375.12 m of the up and down ramps. With an extra 3 m fiber, the total lengths are measured to be 45,380.43 m and 45,379.49 m for the up and down ramps. Thus, the extra fiber lengths are calculated to be 3.61 m and 4.37 m. Compared with the results of shorter FUT, the demodulation spectrum has the following changes. (1) The wings of the spectrum are broadened and side peaks appear, which causes the inaccurate measured length and resolution. The reason may be the nonlinear error accumulation where the wings are broadened as the time delay increases. The expanded spectrum is multiplied with the Fourier transform of the time window, resulting in the side peaks in Figs. 8(d) and 8(g). (2) The SNR has been decreased from 70 dB of 350 m to 19 dB of 45 km. The decrease of SNR is mainly from spectral broadening. In Figs. 8(b) and 8(e), the SNR is limited by the noise floor of −103 dBm that is the quantization noise of the data acquisition card. However, with longer length measurement, the noise floor is raised by the broadened spectrum, which reduces the SNR. (3) There are periodic interference fringes in the background, as shown in Figs. 8(d) and 8(g), but the period is different for the up and down ramps. This is because the durations of the up and down ramps are not strictly the same, so the time window of the fast Fourier transform (FFT) should be selected accordingly, which has about a 5% difference
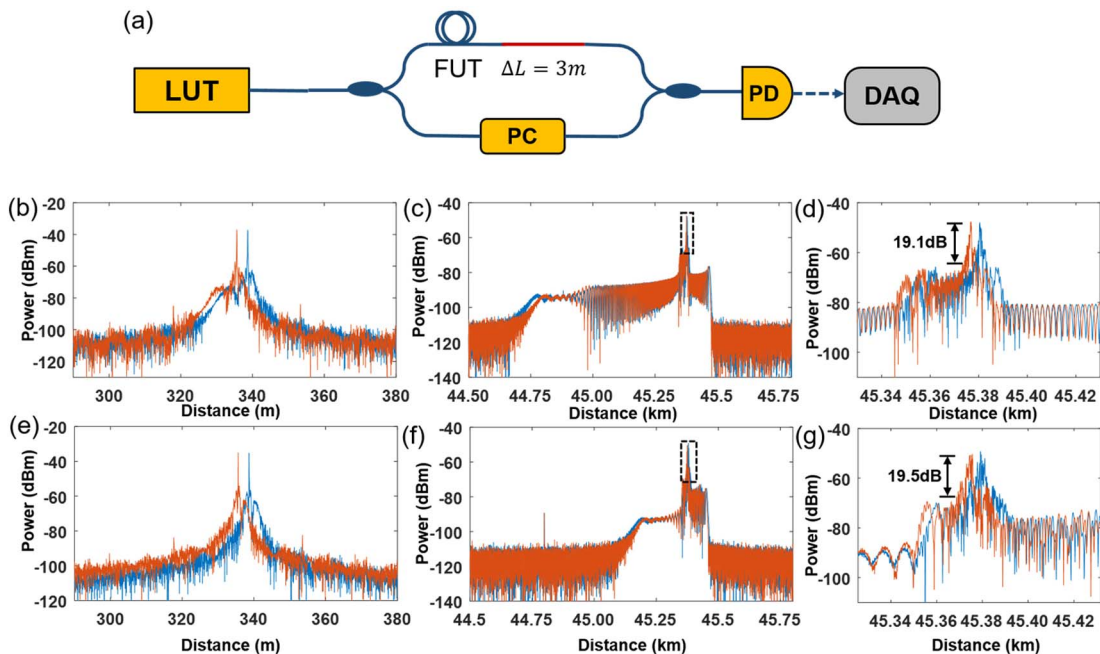

Fig. 8. (a) Experimental setup for performance evaluation of FMCW laser source. FUT, fiber under test; DAQ, data acquisition card. (b)–(g) Demodulated fiber distance which is calculated only by fast Fourier transform (FFT) of the beat signal from the DAQ. The red curve and blue curve represent the result with a fiber length difference of 3 m. The experimental results of 340 m long fiber of (b) up and (e) down ramps with 1 kHz chirped frequency. The experimental results of 45 km long fiber of (c), (d) up and (f), (g) down ramps with 1 kHz chirped frequency where (d), (g) are the enlarged view of the peak frequency in (c), (f), respectively.

between the up and down ramps. It should be noted that the above results merely use the FFT with a rectangular window function to process the raw data without averaging algorithms and other compensation methods such as auxiliary MZI. If more advanced algorithms are applied, the performance of the FMCW laser source will be further improved [38].

5. DISCUSSION

The phase-MRR two-dimensional tuning method for extensive bandwidth frequency modulation overcomes the limitation in the self-injection locked state. The ultra-low frequency noise enables an ultra-long-distance measurement and high linearity provides more accurate distance resolution without compensation algorithms. It can distinguish the length of 3 m difference at 45 km distance. However, the dynamic range is limited by the thermo-optic feature. The frequency bandwidth decreases with the increase of chirped speed. Indeed, for the sake of insurance, we only chose 20 GHz of the static bands for the base of the dynamic FMCW range. Unfortunately, the FMCW source still failed to realize the same tuning range as the static operation, which is even worse at a relatively high chirped frequency when the bandwidth is reduced to 5.6 GHz at 1 kHz chirped frequency. The pre-distortion requires an overload driving voltage signal, which is a heavy power consumption that cannot be ignored. The 20 GHz offset tuning requires the heater driving powers of 304 mW and 252 mW of the phase and MRR, so if the FMCW source wants to achieve more wide sweep bandwidth, a higher-power driving source needs to be prepared, and the trouble of mode hopping should be considered. The proposed on-chip FMCW laser source has a fiber coupling optical power of 0 dBm. If it wants to be used in a space LiDAR measurement system, the master oscillator power amplifier system needs to be used to amplify the power [39]. So the proposed FMCW laser source can improve the SNR of the echo signal, while it also has limitations in the application calling for fast modulated speed and high optical power, such as 3D object imaging [40].

6. CONCLUSIONS

A hybrid integrated on-chip FMCW laser source based on self-injection is proposed. The static tuning range is up to 42 GHz with 49.9 Hz intrinsic linewidth and dynamic FMCW experiment achieves 10.3 GHz bandwidth at 100 Hz chirped frequency and 5.6 GHz bandwidth at 1 kHz chirped frequency by two-dimensional thermal tuning. The generated microwave waveform has a large TBWP up to 5.1×10^7. The iterative learning pre-distortion linearization is employed to realize linearity of $1 - R^2 < 3.0 \times 10^{-8}$, which achieves a resolution of 3 m at a 45 km distance without a compensation algorithm. It paves the way for the application of ultra-long-distance fiber sensing and FMCW LiDAR.

Disclosures. The authors declare no conflicts of interest.

Data Availability. Data underlying the results presented in this paper are not publicly available at this time but may be obtained from the authors upon reasonable request.

REFERENCES

1. C.-H. Yang, Y. Zhang, C.-F. Jin, L. Xu, X. Yang, Q. Wang, Y.-H. Liu, and Y. J. Zhao, "A scheme of pulse compression lidar with enhanced modulated bandwidth for detection through scattering media," Opt. Commun. **381**, 205–209 (2016).
2. X. Zhang, J. Pouls, and M. C. Wu, "Laser frequency sweep linearization by iterative learning pre-distortion for FMCW LiDAR," Opt. Express **27**, 9965–9974 (2019).
3. P. Zhou, F. Zhang, Q. Guo, and S. J. Pan, "Linearly chirped microwave waveform generation with large time-bandwidth product by optically injected semiconductor laser," Opt. Express **24**, 18460–18467 (2016).
4. M. Wegmuller, J. Von Der Weid, P. Oberson, and N. Gisin, "High resolution fiber distributed measurements with coherent OFDR," in ECOC'00 (2000), p. 109.
5. D. F. Pierrottet, F. Amzajerdian, L. Petway, B. Barnes, G. Lockard, and M. J. Rubio, "Linear FMCW laser radar for precision range and vector velocity measurements," MRS Online Proc. Library Archive **1076**, 10760406 (2008).
6. A. Vasilyev, *The Optoelectronic Swept-Frequency Laser and Its Applications in Ranging, Three-Dimensional Imaging, and Coherent Beam Combining of Chirped-Seed Amplifiers* (California Institute of Technology, 2013).
7. R. Huber, M. Wojtkowski, and J. J. Fujimoto, "Fourier domain mode locking (FDML): a new laser operating regime and applications for optical coherence tomography," Opt. Express **14**, 3225–3237 (2006).
8. J. Tang, B. Zhu, W. Zhang, M. Li, S. Pan, and J. J. Yao, "Hybrid Fourier-domain mode-locked laser for ultra-wideband linearly chirped microwave waveform generation," Nat. Commun. **11**, 3814 (2020).
9. H. Gao, C. Lei, M. Chen, F. Xing, H. Chen, and S. Xie, "A simple photonic generation of linearly chirped microwave pulse with large time-bandwidth product and high compression ratio," Opt. Express **21**, 23107–23115 (2013).
10. W. Liang, V. Ilchenko, D. Eliyahu, A. Savchenkov, A. Matsko, D. Seidel, and L. J. Maleki, "Ultralow noise miniature external cavity semiconductor laser," Nat. Commun. **6**, 7371 (2015).
11. R. Tkach and A. R. Chraplyvy, "Regimes of feedback effects in 1.5-µm distributed feedback lasers," J. Lightwave Technol. **4**, 1655–1661 (1986).
12. B. E. Little, S. T. Chu, H. A. Haus, J. Foresi, and J.-P. Laine, "Microring resonator channel dropping filters," J. Lightwave Technol. **15**, 998–1005 (1997).
13. M. Yousefi, D. Lenstra, G. Vemuri, and A. P. A. Fischer, "Control of nonlinear dynamics of a semiconductor laser with filtered optical feedback," IEE Proc. Optoelectron. **148**, 233–237 (2001).
14. M. Yousefi and D. Lenstra, "Dynamical behavior of a semiconductor laser with filtered external optical feedback," IEEE J. Quantum Electron. **35**, 970–976 (1999).
15. Y. Liu, P. Davis, Y. Takiguchi, T. Aida, S. Saito, and J.-M. Liu, "Injection locking and synchronization of periodic and chaotic signals in semiconductor lasers," IEEE J. Quantum Electron. **39**, 269–278 (2003).
16. G. A. Acket, D. Lenstra, A. J. Denboef, and B. H. Verbeek, "The influence of feedback intensity on longitudinal mode properties and optical noise in index-guided semiconductor-lasers," IEEE J. Quantum Electron. **20**, 1163–1169 (1984).
17. D. J. Blumenthal, R. Heideman, D. Geuzebroek, A. Leinse, and C. Roeloffzen, "Silicon nitride in silicon photonics," Proc. IEEE **106**, 2209–2231 (2018).
18. D. Althausen, D. Müller, A. Ansmann, U. Wandinger, H. Hube, E. Clauder, and S. J. Zörner, "Scanning 6-wavelength 11-channel aerosol lidar," J. Atmos. Ocean. Technol. **17**, 1469–1482 (2000).
19. J. F. Bauters, M. J. Heck, D. John, D. Dai, M.-C. Tien, J. S. Barton, A. Leinse, R. G. Heideman, D. J. Blumenthal, and J. E. Bowers, "Ultra-low-loss high-aspect-ratio Si₃N₄ waveguides," Opt. Express **19**, 3163–3174 (2011).

20. L. Tang, Y. Li, J. Li, S. Yang, H. Chen, and J. E. Chen, "Temperature-insensitive Mach–Zehnder interferometer based on a silicon nitride waveguide platform," Opt. Express **45**, 2780–2783 (2020).

21. L. Tang, J. Li, S. Yang, H. Chen, and M. Chen, "A method for improving reflection tolerance of laser source in hybrid photonic packaged micro-system," IEEE Photonics Technol. Lett. **33**, 465–468 (2021).

22. J. Li, B. Zhang, S. Yang, H. Chen, and M. Chen, "Robust hybrid laser linewidth reduction using Si₃N₄-based subwavelength hole defect assisted microring reflector," Photon. Res. **9**, 558–566 (2021).

23. L. Chrostowski and M. Hochberg, *Silicon Photonics Design: From Devices to Systems* (Cambridge University, 2015).

24. D. Huang, M. A. Tran, J. Guo, J. Peters, T. Komljenovic, A. Malik, P. A. Morton, and J. E. Bowers, "High-power sub-kHz linewidth lasers fully integrated on silicon," Optica **6**, 745–752 (2019).

25. L. Columbo, J. Bovington, S. Romero-Garcia, D. F. Siriani, and M. Gioannini, "Efficient and optical feedback tolerant hybrid laser design for silicon photonics applications," IEEE J. Sel. Top. Quantum Electron. **26**, 8301210 (2019).

26. M. A. Tran, D. Huang, and J. E. Bowers, "Tutorial on narrow linewidth tunable semiconductor lasers using Si/III-V heterogeneous integration," APL Photonics **4**, 111101 (2019).

27. J. W. Dawson, N. Park, and K. J. Vahala, "An improved delayed self-heterodyne interferometer for linewidth measurements," IEEE Photonics Technol. Lett. **4**, 1063–1066 (1992).

28. S. Camatel and V. Ferrero, "Narrow linewidth CW laser phase noise characterization methods for coherent transmission system applications," J. Lightwave Technol. **26**, 3048–3055 (2008).

29. L. B. Mercer, "1/f frequency noise effects on self-heterodyne linewidth measurements," J. Lightwave Technol. **9**, 485–493 (1991).

30. P. Gallion, H. Nakajima, G. Debarge, and C. Chabran, "Contribution of spontaneous emission to the linewidth of an injection-locked semiconductor laser," Electron. Lett. **21**, 626–628 (1985).

31. L. Stern, W. Zhang, L. Chang, J. Guo, C. Xiang, M. A. Tran, D. Huang, J. D. Peters, D. Kinghorn, and J. E. Bowers, "Ultra-precise optical-frequency stabilization with heterogeneous III–V/Si lasers," Opt. Lett. **45**, 5275–5278 (2020).

32. L. Tang, S. Shao, S. Yang, H. Chen, and M. Chen, "Frequency modulated continuous wave narrow linewidth laser diode based on self-injection locking with external micro-ring resonator," in *European Conference of Integrated Optics (ECIO)* (2020), pp. 1–3.

33. M. Kamoun, R. K. Zadeh, Z. Zhao, G. Yang, and H. Bao, "Radio over fiber for cellular networks: system identification and pre-distortion strategies," in *IEEE Wireless Communications and Networking Conference (WCNC)* (2019), pp. 1–6.

34. H.-S. Ahn, Y. Chen, and K. L. Moore, "Iterative learning control: brief survey and categorization," IEEE Trans. Syst. Man Cybern. C **37**, 1099–1121 (2007).

35. M. Han and B. Mheen, "High-resolution remote range detection method based on uncompensated FMCW sources for low-cost FMCW LIDAR," Proc. SPIE **11525**, 1152523 (2020).

36. A. Dieckmann, "FMCW-LIDAR with tunable twin-guide laser diode," Electron. Lett. **30**, 308–309 (1994).

37. S. O. Piper, "FMCW linearizer bandwidth requirements," in *IEEE National Radar Conference* (1991), pp. 142–146.

38. X. Fan, Y. Koshikiya, and F. J. Ito, "Phase-noise-compensated optical frequency domain reflectometry with measurement range beyond laser coherence length realized using concatenative reference method," Opt. Lett. **32**, 3227–3229 (2007).

39. M. Liang, Q. Liu, and W. Hu, "1550 nm monolithic MOPA diode laser for Lidar applications," Proc. SPIE **11182**, 1118207 (2019).

40. A. Martin, D. Dodane, L. Leviandier, D. Dolfi, A. Naughton, P. O'Brien, T. Spuessens, R. Baets, G. Lepage, and J. Verheyen, "Photonic integrated circuit-based FMCW coherent LiDAR," J. Lightwave Technol. **36**, 4640–4645 (2018).